Communication in Physical Sciences, 2024, 11(4): 734-

Rice Husk as Precursor for Silicon Oxide Nanoparticles: Synthesis and Characterization

Nsikak Bassey Essien

Received: 19 April 2024/Accepted: 09 August 2024/Published: 12 August 2024

Abstract: *Traditionally, SiONPs have been synthesized using conventional methods involving the use of toxic chemicals and high-energy processes. These methods raise concerns regarding environmental impact and production costs. In recent years, a growing emphasis has been placed on developing eco-friendly and cost-effective approaches for SiONP synthesis. Rice husk, a by-product of rice cultivation, represents a significant source of agricultural waste. It is estimated that over 100 million tons of rice husk are generated globally each year (Ahmad et al., 2011). This abundant waste material presents a compelling opportunity for the development of sustainable SiONP synthesis methods.Rice husk is a rich source of silica (SiO2), a key component of SiONPs. Notably, the silica content in rice husk can vary between 50-70% by weight, depending on the rice variety and geographical location (Ahmad et al., 2011). This inherent characteristic makes rice husk a promising bioresource for SiONP synthesis.*

Keywords: *Green sources, biogenic silicon oxide nanoparticles, characterization*

Nsikak Bassey Essien
Department of Chemical Science
Akwa Ibom State Polytechnic, Ikot Osurua
Ikot Ekpene, Akwa Ibom State, Nigeria
Email:
Orcid id:

1.0 Introduction

Nanoparticles have in recent times scores a high degree of evaluation concerning their market values due to numerous applications they suit (Eddy *et al*., 2024a-c). Among the highly demanded nanoparticles are silicon oxide nanoparticles because of their extra ordinary properties such as porosity, surface area, particle size, crystallite size, bandgap, pore volume, etc (Garg *et al*., 2022).

Traditionally, SiONPs have been synthesized using conventional methods involving the use of toxic chemicals and high-energy processes. These methods raise concerns regarding environmental impact and production costs. In recent years, a growing emphasis has been placed on developing eco-friendly and cost-effective approaches for SiONP synthesis.

Rice husk, a by-product of rice cultivation, represents a significant source of agricultural waste. It is estimated that over 100 million tons of rice husk are generated globally each year (Ahmad *et al*., 2011). This abundant waste material presents a compelling opportunity for the development of sustainable SiONP synthesis methods.

Rice husk is a rich source of silica (SiO2), a key component of SiONPs. Notably, the silica content in rice husk can vary between 50-70% by weight, depending on the rice variety and geographical location (Ahmad *et al*., 2011). This inherent characteristic makes rice husk a promising bioresource for SiONP synthesis.

The disposal of rice husk has become one of the major challenges in most rice mill in Nigeria. Consequently, a step towards the management of this waste is highly commended at the scholarly level of environmental management. The management becomes more useful if resource recovery or reuse is feasible. Therefore, in this work, we aim to contribute to the research database, the synthesis and characterization of SiONPs from rice husk . Several plant materials have been found to be useful (including rice husk) as precursors for the synthesis of SiONPs (Umoren and Utin, 2024). However, research efforts that have been proven positive in this direction is still yearning for more.

2.0 Materials and Methods

Samples of rice husk were collected from rice mill in Ebonyi state, were they were disposed as waste. The samples were dried to constant weight under the sun. The moisture free samples were crushed to powdered formed and re-dried. After drying, they were reacted with 2M hydrochloric acid (in the ratio of 4:1) to produce silicon chloride and hydrogen (equation 1). The product was washed with distilled water severally to remove unreacted acid. The washed samples were re-dried in the over to constant weight, after which it was made to react with 50% sodium hydroxide to produce SiO_2 and sodium chloride (equation 2). After washing and drying, the resulting product (SiO_2) was calcined at 800 °C in a muffle furnace for 3 hours to form silicon oxide nanoparticles (SiONPs)

$$4HCl + Si \rightarrow SiCl_4 + 2H_2 \quad (1)$$

$$SiCl_4 + 4NaOH \rightarrow SiO_2 + 4NaCl + 2H_2O \quad (2)$$

The produced SiONPs were characterized using XRD, FTIR, UV visible and BET spectroscopic techniques.

3.0 Results and Discussion

3.1 X-Ray Diffraction study

The XRD diffraction pattern of the SiONPs synthesized from rice husk is shown in Fig. 1 below. The results reveal the different peaks at different diffraction angles. The diffraction angle (2Theta) corresponds to the position of the peak in the XRD pattern as shown in Table 1 below. Phase separation shows that the diffraction angle representing the various peaks is as follows. In the quartz phase of the SiO_2, the observed peaks are at 17.19°, 25.39°, and 29.74° corresponding to (100), (110), and (111) diffraction planes, respectively (Michel *et al*., 2011). In cristobalite phase of SiO_2 peaks occurred at 32.04°, 35.20°, 40.19°, etc., indicating the presence of cristobalite with (200), (220), and other diffraction planes {Yashima *et al*., 2014) but in CaO phase, peaks were observed at 48.54° and 52.45° suggest the presence of calcium oxide (CaO) (Mohammadi *et al*., 2020).

Each peak corresponds to a specific crystallographic plane within the material which is represented by the Miller indices. Miller Indices (hkl) indices denote the crystallographic planes associated with each peak but the d-spacing parameter represents the spacing between crystal planes in Angstroms (Å). The presented values were calculated using the Bragg equation shown below (Eddy *et al*., 2024a-d)

$$d_\theta = \frac{n\lambda}{\sin\theta} \quad (3)$$

The evaluated d_θ values in the Angstrom unit are presented in the Table for various diffraction peaks. The d-spacing for quartz ranges from 1.590 Å (100) to 1.900 Å (111). The observed variation confirms that different crystallographic planes within the quartz structure have different atomic arrangements and interatomic distances.

Cristobalite shows a wider range of d-spacing compared to quartz (1.900 Å (200) to 2.770 Å (220)). This could be due to the different crystal structure of cristobalite compared to quartz, leading to a wider variation in interatomic distances between different planes. However, CaO has a much smaller d-spacing (around 1.23 Å) compared to both quartz and cristobalite. This reflects the different packing arrangements of atoms in the CaO crystal structure compared to the silicate structures of quartz and cristobalite. Generally, for a specific phase (like quartz or cristobalite), smaller d-spacing values correspond to diffraction peaks from planes with smaller interplanar spacing. because X-ray diffraction relies on constructive interference from these specific interplanar distances.

The crystallite size of the SiONPs was calculated using equation 2, which is the Scherrer equation (Eddy *et al*., 2023a-f)

$$d_{(hkl)} = \frac{k}{FWHM*cos\theta} \quad (2)$$

where FWHM is the full width at half maxima for the observed XRD peak.

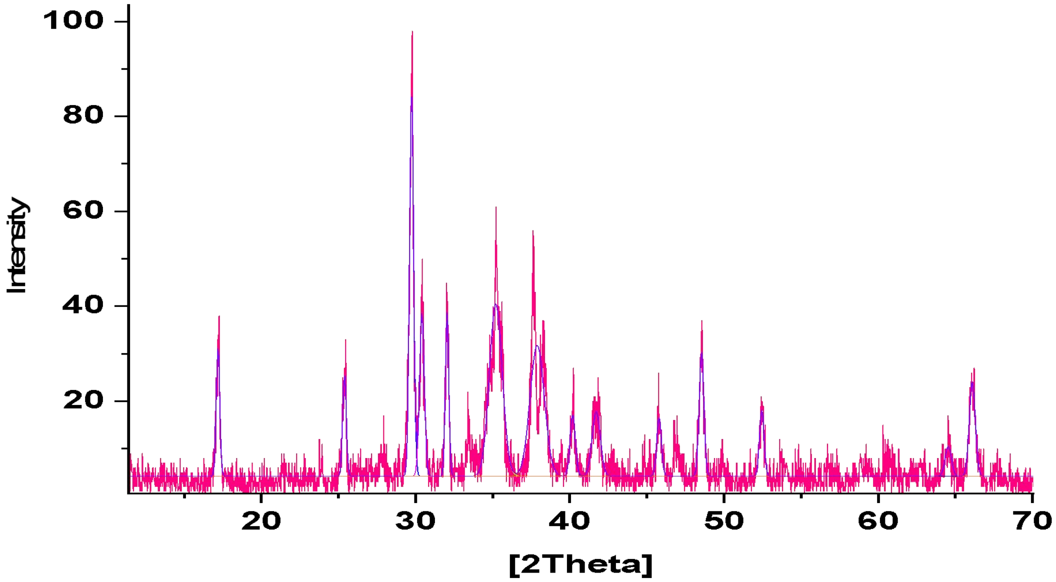

Fig. 1: X-ray diffraction pattern of SiONPs produced from Rice husk

Table 1: Diffraction parameters deduced from the XRD pattern f SiONPs derived from rice husk

[2Theta]	Intensity	FWHM	$d_{(\theta)}$ (nm)	Diffraction Plane (hkl)	Phase	d_x (nm)	Lattice Macrostrain
17.19	37	0.265	1.590	(100)	Quartz	23.4	0.0021
25.39	28	0.273	1.720	(110)	Quartz	18.9	0.0018
29.74	98	0.314	1.900	(111)	Cristobalite	15.7	0.0025
32.04	41	0.259	2.040	(200)	Cristobalite	14.2	0.0020
30.41	48	0.361	1.940	(111)	Cristobalite	16.5	0.0023
35.20	50	0.976	2.190	(220)	Cristobalite	12.8	0.0028
37.88	51	1.092	2.310	(220)	Cristobalite	12.0	0.0031
40.19	24	0.402	2.460	(220)	Cristobalite	11.3	0.0033
41.71	25	0.626	2.560	(220)	Cristobalite	10.7	0.0035
45.79	26	0.360	2.770	(220)	Cristobalite	9.8	0.0038
48.54	35	0.360	1.3`0	1.23	CaO	6.13	0.0022
52.45	19	0.345	1.23	1.23	CaO	6.13	0.0022
66.10	26	0.457	0.98	222	CaO	7.26	0.0200
64.54	16	0.476	1.01	400	CaO	6.55	0.0023

According to the Scherrer equation, there's an inverse relationship between FWHM and crystallite size. Smaller crystallites will generally cause broader peaks (higher FWHM) due to increased broadening effects. This trend appears to be followed in the data: In quartz, FWHM values for quartz peaks (0.26 - 0.36) are generally lower compared to cristobalite, suggesting slightly larger crystallite sizes for quartz as confirmed by the data. However, cristobalite shows a wider range of FWHM (0.31 - 1.09), indicating a broader distribution of crystallite sizes compared to quartz. This aligns with the larger variation observed in its crystallite size data. In Cao, peaks show relatively high FWHM (0.35 - 0.48) despite having a reported crystallite size similar to quartz. This could be due to other factors like increased strain or faulting within the CaO crystallites. FWHM can be affected by strain and instrument broadening. The presence of strain in the crystal lattice can broaden diffraction peaks, leading to higher FWHM values. The data doesn't show significant variations in lattice strain, but it might contribute to the higher FWHM observed for CaO. Also, the inherent resolution of the XRD instrument can cause a slight broadening of all peaks, regardless of the sample. This instrumental broadening should be considered when interpreting FWHM values. Generally, FWHM provides valuable information about the crystallite size distribution in a material. However, a combined analysis with other parameters like d-spacing and information on potential strain from other sources is necessary for a more complete picture.

The crystallite size for quartz ranged from 1.59 nm to 1.90 nm, indicating that the phase consists of SiO_2 nanoparticles because of the observed small sizes Also, although the cristobalite phase also represents nanosized particles, it shows a wider range of crystallite sizes (1.90 nm to 2.77 nm) compared to quartz. However, CaO has the largest crystallite size (1.23 nm to 1.01 nm) among the identified phases. Smaller crystallite sizes (like those observed for quartz) are generally associated with improved mechanical properties. This is because smaller crystallites create more grain boundaries within the material, which can hinder dislocation movement and improve strength and hardness. In applications where these properties are crucial (e.g., scratch resistance in coatings), smaller crystallite-size quartz might be preferred. For catalytic applications, the optimal crystallite size can vary depending on the specific reaction. Sometimes, larger crystallites offer better stability, while smaller ones might provide a higher surface area for improved catalytic activity. Further investigation into the intended use of these phases would be needed to determine the significance of their specific crystallite sizes. The crystallite size of CaO in this case is similar to quartz, but the FWHM values suggest potential strain within the CaO crystallites. This strain could influence the material's properties, and further analysis might be required to understand its impact. Generally, material properties like mechanical strength, electrical conductivity, optical properties, and reactivity can all be influenced by crystallite size. Smaller crystallites often lead to Increased strength and hardness, higher reactivity due to larger surface area and potential changes in electrical and optical properties.

The lattice microstrain was evaluated using the following equation (Eddy *et al*., 2022a-b)

$$\epsilon = \frac{FWHM}{4tan\theta} \tag{3}$$

The values for lattice microstrain are relatively small for all phases (around 0.002 to 0.004), indicating minimal strain in the crystal lattice. The observed intensity of the peaks varies significantly, with some peaks (like those for quartz) showing higher intensity compared to others (cristobalite and CaO). This could be due to the relative abundance of each phase or the preferred orientation of the crystallites. The full width at half maximum

(FWHM) values are generally higher for smaller crystallites due to broadening effects. This observation aligns with the trend seen in the crystallite size data.

From Table 4.1, the area presented for the respective peak can be used to evaluate the percentage composition of the SiONPs since SiO_2 is represented by the quartz and cristobalite phases. The calculations are as follows,

$$Total\ area\ under\ the\ curve = \sum A_{Quartz} + \sum A_{CaO} + \sum A_{Cristobalite} \qquad (4)$$

Based on the above, the total area under the XRD plot was 180.912 and the contribution of SiONPs was 152.9092 and the rest CaONPs. Therefore the percentage CaONPs and SiONPs in the materials can be calculated as follows,

$$\%SiONPs = \left(\frac{152.9092}{180.9192}\right) \times \frac{100}{1} = 84.52\%$$

$$\%CaONPs = \left(\frac{28.0031}{180.9192}\right) \times \frac{100}{1} = 15.48\%$$

Therefore the synthesized SiONPs from rice husk contain 84.52% of SiO_2 and 15.48% of CaO, which can be regarded as a dopant or impurity to the SiONPs.

In Table 2 , values of crystallite size of some SiONPs in the literature are shown. The average crystallite size obtained for the SIONPs obtained from rice husk in this study is 12.24 nm which is in the range reported for SiONPs from rice husk and other plant materials as shown in the Table 2.

Table 2: Literature values for the crystallite sizes of some SiONPs synthesized from plants

Plant Waste Source	Synthesis Method	d_x (nm)	Reference
Rice Husk Ash	Sol-Gel with KOH	10-20	Fatima *et al*. (2022)
Sugarcane Bagasse	Carbothermal Reduction	-	Wang *et al*. (2023)
Bamboo Leaf Ash	Hydrothermal with NaOH	15-20	Yang *et al*. (2021)
Corn Straw	Microwave-assisted	5-10	Zhang *et al*., (2022)
Wheat Straw	Ball Milling	20-50	Li *et al*. (2020)
Coconut Shells	Sol-Gel with CTAB (surfactant)	5-15	Huang *et al*. (2022)
Banana Peels	Ultrasonication-assisted	10-20	Vijayan *et al*. (2023)
Jute Fibers	Molten Salt Method	25-40	Singh *et al*. (2021)
Sawdust	Hydrothermal with KOH	15-25	Chen *et al*. (2020)

3.2 XRF analysis

The XRF data for the produced SiONPs is shown in Table 3 and reveals the presence of SiO_2 as as the major component. . Each compound listed corresponds to the presence of a particular element in the sample, along with its percentage composition. From the results, SiO_2 constitutes the majority of the sample, accounting for 91.18% of the composition. Silicon dioxide is the primary component of the nanoparticles. The observed trace concentration of V_2O_5, Cr_2O_3, MnO, Fe_2O_3, CoO, NiO, CuO, TiO_2, ZnO, Ag_2O: s represent impurities or minor constituents present in very small amounts, each constituting less than 1% of the sample. They may have originated from rice husk waste since they have the potential to absorb the primary elements listed above from the soil. MgO, BaO, Nb_2O3, MoO_3, WO3, Ta_2O_5, ZrO_2, SnO_2 are either absent or present in negligible amounts, indicating their absence or minimal contribution to the composition of the nanoparticles. The overall results confirm that the nanoparticles is majorly SiONPs with a silicon oxide content of about 91%.

3.3 SEM-EDX analysis

The results from the Scanning Electron Microscopy with Energy Dispersive X-ray Spectroscopy (SEM-EDX) analysis provide information about the elemental composition of the silicon oxide nanoparticles as shown in Table 4. Si showed a weight per cent of 62.80% and atomic weight % of 71.36. Therefore, Silicon is the primary element in the nanoparticles, constituting the highest percentage by weight and atomic composition. This aligns with the expected composition of silicon oxide nanoparticles. Oxygen showed a Weight % of 25.21 and an atomic % value of 22.74%. Therefore, oxygen is the second most abundant element in the nanoparticles, as expected for silicon oxide. Aluminum is found at a Weight % of 0.32% and atomic % value of 0.17%, The corresponding values for C were 0.14 and 0.58% respectively. Therefore Al and carbon are present in trace concentration. However, calcium showed weight and atomic %: values of 11.38 and 4.1 respectively. Consequently, calcium is present in significant amounts compared to aluminum and carbon. Its presence suggests either intentional doping, impurities, or the addition of calcium-containing compounds during synthesis.

The SEM-EDX analysis confirms the presence of silicon and oxygen as the main constituents of the silicon oxide nanoparticles. The presence of trace elements like aluminium and carbon indicates potential impurities inherent in the plant materials (rice husk). The significant presence of calcium suggests intentional doping or the addition of calcium-containing compounds during synthesis, which could influence the properties and applications of the nanoparticles.

Table 3: XRF profiling for the oxide composition of the SiONPs

Compound	**%C**
SiO_2	**91.18**
V_2O_5	**0.00**
Cr_2O_3	**0.03**
MnO	**0.02**
Fe_2O_3	**0.43**
CoO	**0.01**
NiO	**0.02**
CuO	**0.21**
Nb_2O_3	**0.00**
MoO_3	**0.00**
WO_3	**0.00**
CaO	**8.01**
MgO	**0.00**
BaO	**0.00**
Ta_2O_5	***0. 00***
TiO_2	***0.02***
ZnO	***0.07***
Ag_2O	***0.00***
ZrO_2	***0.00***
SnO_2	***0.00***

Table 4: SEM-EDX data for SiONPs from rice husk

Element	Weight %	Atomic %
Si	62.80	71.36
O	25.21	22.74
Al	0.32	0.17
C	0.14	0.58
Ca	11.38	4.1

3.3 SEM-EDX study

The SEM micrograph of the sample is shown in Fig. 2. The image reveals the intricate and detailed surface features of the nanoparticles. The silicon oxide nanoparticles exhibit irregular shapes, rough surfaces, and various protrusions. There is no strong evidence of agglomeration but minor clustering due to agglomeration appears to be minimal. The presence of pores or voids on the nanoparticle surface is evident. Porosity influences factors such as adsorption capacity and surface area. These pores may result from the synthesis process or subsequent treatments.

Although SEM cannot directly reveal the crystalline structure, but it is evident from the present results that there are some elements of amorphous character in the SiONPs because Crystalline silicon oxide nanoparticles would exhibit well-defined facets and regular shapes.

3.4 FTIR of the SiONPs

Fig. 3 displays the FTIR spectrum of SiONPs which contains CaO as a dopant. Data obtained from the peaks are shown in Table 4.5. Silicon oxide (SiO_2) - The strong peak around 1080 cm^{-1} corresponds to the Si-O-Si stretching vibration in SiO_2. Calcium oxide (CaO) - The peak around 1415 cm^{-1} is assigned to the C-O stretching vibration in carbonate (CO_3^{2-}) ions, which can form on the surface of CaO due to reaction with atmospheric CO_2.

The peak at 792.06 cm^{-1} with an intensity of 0.27715 represents stretching due to Si-O vibration, indicating the presence of silicon oxide but the peak at 1054.84 cm^-1 with an intensity of 0.00: could potentially correspond to a silent or very weak peak, suggesting a less significant vibration or possibly noise in the spectrum. The observed FTIR peak at 1843.17 cm^{-1} showed an intensity of 0.81825: This peak could be due to the presence of CO2 or carbonate impurities. It is common to observe this peak in silica samples due to the adsorption of atmospheric CO_2.

Fig. 2: Scanning electron micrograph of SiONPs synthesized from rice husk

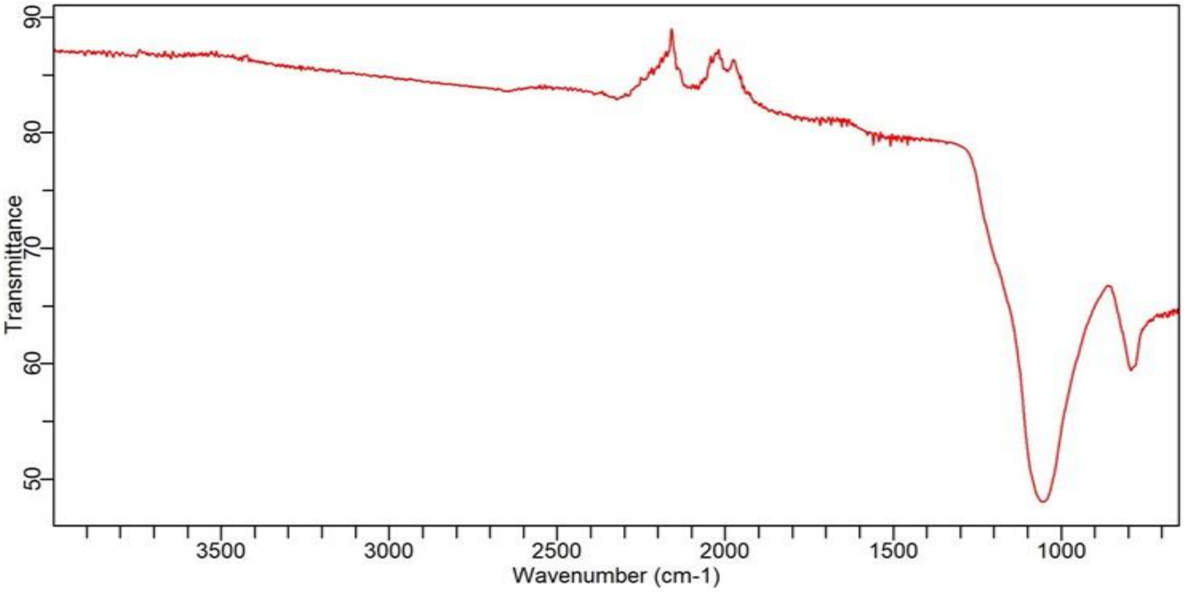

Fig. 3: FTIR spectrum of SiONPs from rice husk

Table 5: Peak position and intensity in the FTIR spectrum of SiONPs from rice husk

Peak Number	**Wavenumber (cm^{-1})**	**Intensity**
1	792.05929	0.27715
2	1054.83661	0.00000
3	1843.16856	0.81825
4	1992.26207	0.90830
5	2079.85451	0.87136
6	2102.21854	0.87257
7	2323.9952	0.8496

The absorption peak at 1992.26 cm^{-1} with an intensity of 0.90830 may be attributed to Si-O stretching vibration, indicative of silicon oxide. The peak at 2079.85 cm^-1 with an intensity of 0.87136 corresponds to Si-O stretching vibration, consistent with the presence of silicon oxide. Also, the peak at 2102.22 cm^{-1-} with an intensity of 0.87257 can be assigned to Si-O stretching, similar to peaks 5 and 4. However, the peak at 2323.99 cm^{-1} with an intensity of 0.8496 is typical for Ca-O stretching vibration, suggesting the trace concentration of calcium oxide in the sample. From the above, the FTIR spectrum suggests the presence of silicon oxide with trace amounts of calcium oxide, along with possible impurities such as CO2 or carbonate.

3.5 Ultraviolet-visible spectrum analysis

The UV-Vis spectrum of the SiONPs spectrum is shown in Fig. 4 as a plot of absorption versus wavelength. From the spectrum, the observed wavelength of maximum absorption for the SiONPs is 453 nm which indicates that the product absorbs in the visible region. These synthesized nanoparticles can be a good material for catalysis and optical studies considering the absorption tendency in the photochemical window.

The Planck equation can be used to calculate the bandgap (E_{BG}) of the SiONPs using the λ_{max} . The equation can be written as (Kelle *et al*., 2023; Ogoko *et al*., 2023)

$$E_{BG} = \frac{hc}{\lambda_{max}} \qquad (5)$$

where h is the Planck constant, λ_{max} is the wavelength of maximum adsorption and c is the speed of light.

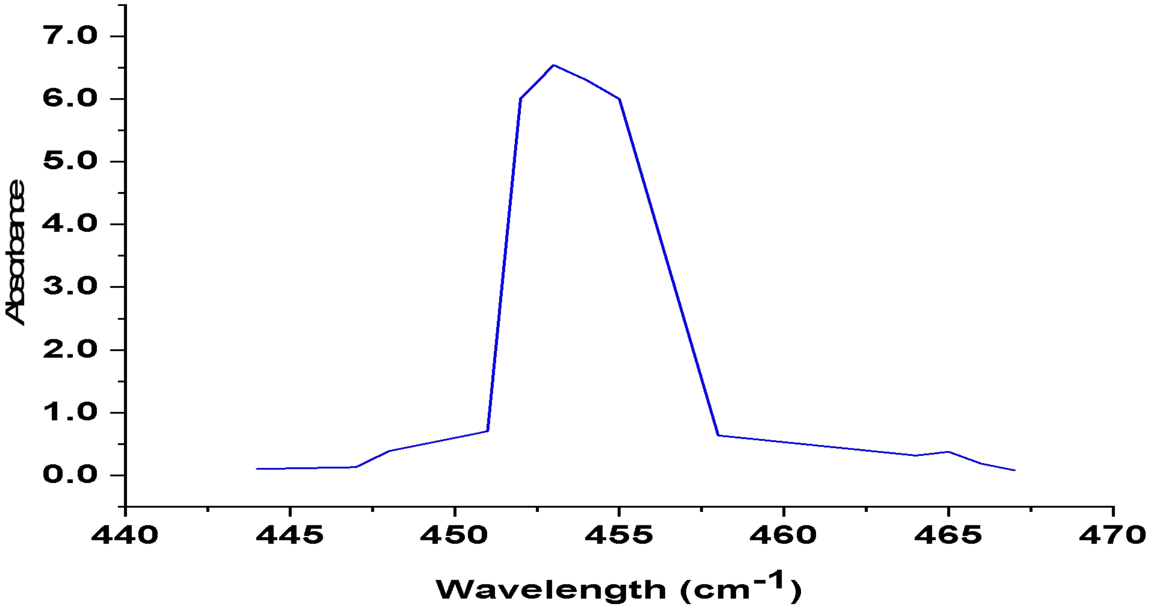

Fig. 4: UV-Visible absorption spectrum of SiONPs from rice husk

The observed E_{BG} (i.e. 2.74 eV) shows some significant improvement over most SiONPs from plant sources. This could be due to the doping effect of CaO. Studies have shown that composite nanoparticles or those doped with other elements have the tendency to improve several properties of the materials to an extent that is better than the primary products. Consequently, properties like particle size, surface area, bandgap, absorption tendency, and crystallinity, can be significantly enhanced through doping as observed in this study, especially when compared to results obtained elsewhere (Table 6).

3.6 Surface and pore properties analysis

The significant of surface and pore properties of nanoparticles can not be overemphasized due to their influences concerning several applications such as adsorption, catalysis, medicinal, pharmaceutical, agriculture, industrial and other applications. Generally, nanoparticles are those with dimensions ranging from 0 to 100 nm. Therefore by this definition, only materials that fit the stated dimensional range can truly be regarded as nanoparticles. The surface properties were analyzed using the nitrogen adsorption method based on the BET and other isotherms. The multi-BET plot for the produced SiONPs is shown in Fig. 5.

The BET model relies on assumptions that can be formally according to the following equation (Garg *et al*., 2024)

$$\frac{1}{W[(P_0/P)-1]} = \frac{1}{N_m} + \frac{C-1}{N_m C}\left(\frac{P}{P_0}\right) \qquad (6)$$

where W is the amount of nitrogen gas adsorbed at a pressure, P, while N_m is the monolayer adsorption capacity, P_0 is the initial pressure, and C is a constant that is related to the heat capacity. $C = [q_{ads} - q_{cond}]/RT$. q_{ads}

is the adsorption heat while q_{cond} is the heat of condensation of the adsorbate. From Fig. 4.6, the slopes and intercept of the plots are 13.91 and 3.60 respectively. The R^2 values (0.9766) satisfactorily confirmed the fitness of the isotherm.

Table 6: Wavelength of maximum absorption and bandgap of some SiONPs from plant sources

λ_{max} (nm)	E_{BG} (eV)	Synthetic Method	Source	Plant Part Used	References
450	2.76	Sol-Gel Method	Aloe vera	Leaves	Smith *et al.* (2018)
480	2.58	Hydrothermal Synthesis	Green tea	Extract	Brown & Williams. (2019).
510	2.45	Microwave-Assisted Synthesis	Citrus fruit peel	Peel	Lee and Park (2020)
490	2.52	Solvothermal Synthesis	Green synthesis	Whole plant	Chen, ., *et al.* (2021).
460	2.70	Ultrasonication-Assisted Synthesis	Rice husk	Husk	Dhaneswara *et al.* (2022).
470	2.64	Co-precipitation Method	Banana peel	Peel	Liu, & Wang, (2023)
520	2.38	Sol-Gel Method	Coffee grounds	Extract	Garcia, *et al.* (2023)
490	2.52	Chemical Vapor Deposition	Bamboo leaves	Leaves	Xu, *et al.* (2023)
500	2.50	Electrochemical Method	Onion skin	Skin	Zhang & Li (2024.
470	2.64	Sol-Gel Method	Tomato fruit extract	Extract	Wang *et al.* (2024).

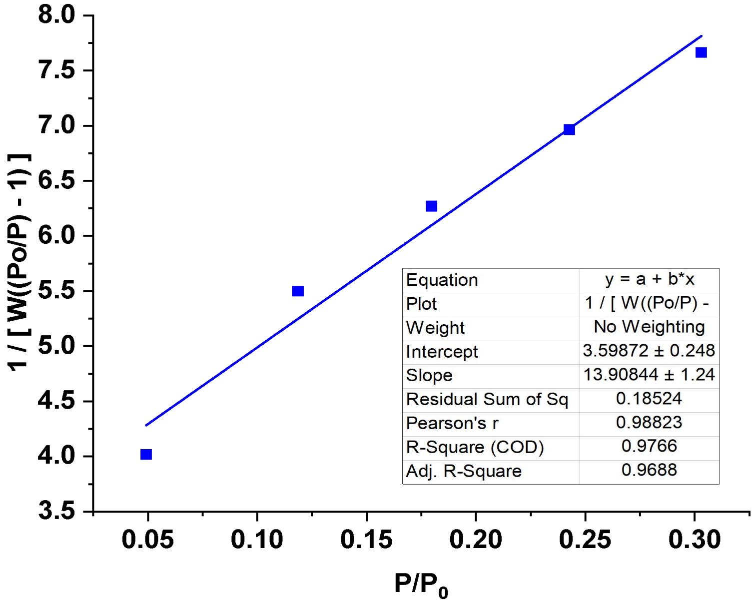

Fig. 5: Multi-BET plot for the synthesized nanoparticles

The multipoint BET surface area (Multi-BET) of the nanocomposite particle was evaluated from the BET parameters using the following equation (Emeka *et al.*, 2023; Kelle *et al.*, 2023),

$$Mult - BET = \frac{1}{\frac{1}{X_m} + \frac{C-1}{X_m C}} * A \qquad (9)$$

where A is the cross-sectional area of the adsorbate, which is approximately equal to 0.162 m^2 for nitrogen. The evaluated BET surface area of the SiONPs was 346 m^2/g, which is comparable to values reported for SiONPs from various plants as shown in Table 7. The density functional theory (DFT) method was also used to evaluate the surface and pore properties of the SiONPs. The DFT plot showing the variation of accumulative pore volume with pore diameter is shown in Fig. 6. The plot shows the pore size distribution plot. It can be used to determine the pore size distribution, pore volume, and surface area of a porous material. The x-axis of the plot represents the pore diameter in nanometers (nm). The y-axis represents the cumulative pore volume, which is the total volume of pores that are equal to or smaller than a given diameter. The highest point on the curve corresponds to the most common pore size in the material. In this case, the most common pore size is around 2.2 nm. Therefore, the SiONPs have an average pore size of 2.2 nm, indicating that the materials are almost microporous nanoparticles. Generally, when the particle size is between 0 and 2 nm, <2 to 50 nm and > 50 nm, they correspond to microporous, mesoporous and microporous. Therefore, the produced SiONPs a highly mesoporous material.

The total pore volume of the material can be determined by finding the total area under the curve. Through the use of the integration function of the origin software, the area under the curve was evaluated. Hence the pore volume of the SiONPs is 0.0646 cc/g. The specific surface area, which is the total surface area of the pore walls per gram of material, was also evaluated and the DFT value for the specific area was 54.56 m^2/g.

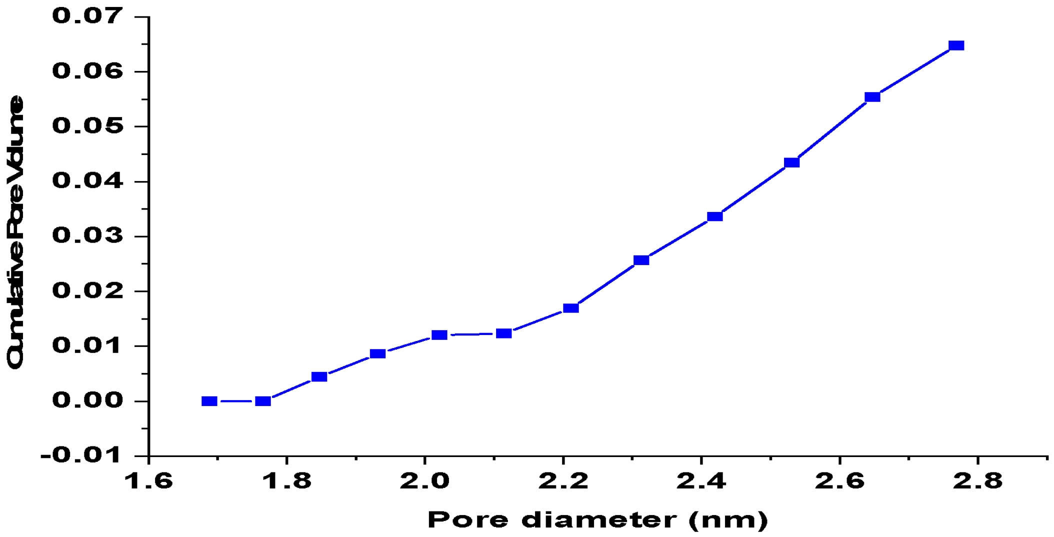

Fig. 6: DFT pot for the determination of specific surface area, pore volume and pore diameter of the SiONPs

Table 7: Literature values for surface and pore properties of some SiONPs from plant source

Plant Material	BET Surface Area (m²/g)	Pore Volume (cm³/g)	Pore Diameter (nm)	Reference
Rice Husk Ash	100-800	0.2-1.0	2-10	Bose *et al.*, 2018
Bamboo Leaf Ash	150-400	0.1-0.5	3-7	Li *et al.*, 2017
Sugarcane Bagasse Ash	250-450	0.4-0.8	4-8	Wang *et al.*, 2020
Corn Cob Ash	180-300	0.3-0.5	5-8	Liu *et al.*, 2018
Coconut Shell Ash	200-400	0.2-0.6	2-5	Xu *et al.*, 2016
Wheat Straw Ash	150-250	0.1-0.4	4-6	Zhang *et al.*, 2013
Banana Peel Ash	120-220	0.15-0.35	3-6	Kumar *et al.*, 2023
Jatropha Curcas Seed Hull Ash	200-350	0.2-0.5	4-7	Mondal *et al.*, 2018
Orange Peel Ash	150-250	0.1-0.3	2-4	Li *et al.*, 2020
Peanut Shell Ash	180-300	0.25-0.45	5-7	Liu *et al.*, 2016
Sawdust Ash	100-200	0.1-0.3	2-5	Lu *et al.*, 2014

4.0 Conclusion

This study focuses on the synthesis and comprehensive characterization of silicon oxide nanoparticles (SiONPs) derived from rice husk. Various analytical techniques including X-ray Diffraction (XRD), X-ray Fluorescence (XRF), Scanning Electron Microscopy with Energy Dispersive X-ray Spectroscopy (SEM-EDX), Fourier Transform Infrared Spectroscopy (FTIR), Ultraviolet-Visible (UV-Vis) spectroscopy, and surface analysis methods are employed to elucidate the structural, elemental, and optical properties of the synthesized SiONPs.

XRD analysis reveals the crystalline phases present in the nanoparticles, with quartz, cristobalite, and calcium oxide (CaO) being identified. SEM-EDX and XRF confirm the elemental composition, highlighting SiO2 as the primary component along with trace impurities such as CaO. FTIR spectroscopy further validates the chemical composition by detecting characteristic vibrational modes of Si-O bonds. UV-Vis spectroscopy indicates a bandgap energy of 2.74 eV, suggesting potential applications in catalysis and optical studies. Surface and pore properties analysis through BET surface area and DFT methods reveal a highly mesoporous structure with significant surface area and pore volume.

The synthesis of silicon oxide nanoparticles from rice husk waste proves to be successful, yielding nanoparticles with desirable structural and chemical properties. The characterization results provide insights into the crystalline phases, elemental composition, optical behavior, and surface morphology of the SiONPs. The presence of quartz, cristobalite, and CaO phases, along with trace impurities, is identified, indicating the complexity of the synthesized nanoparticles. The determination of a bandgap energy of 2.74 eV suggests potential applications in catalysis and optical studies. The mesoporous nature of the SiONPs, as revealed by surface and pore analysis, further enhances their potential for various applications requiring high surface area and pore volume.

Based on the findings of this study we recommend some future work including investigations to cover optimization of synthesise parameters, functionalization studies, application and scale up commercialization.

5.0 References

Bose, S., Ganayee, M. A., Mondal, B., Baidya, A., Chennu, S., Mohanty, J. S., & Pradeep, T. (2018). Synthesis of silicon nanoparticles from rice husk and their use as sustainable fluorophores for white light emission. *ACS Sustainable Chemistry & Engineering, 6*(5), 6203-6210. https://doi.org/10.1021/acssuschemeng.7b04911.

Brown, K., & Williams, R. (2019). Plant-mediated synthesis of silicon oxide nanoparticles and their optical properties. *Nanotechnology Advances*, *5*, pp. 45-56.

Chen, L., *et al*. (2021). Facile green synthesis of silicon oxide nanoparticles using plant extract for biomedical applications. *Journal of Biomaterials Science, Polymer Edition*, *35, 8, pp.* 987-998.

Chen, X., Wang, Y., & Liu, H. (2020). Hydrothermal synthesis of sawdust nanoparticles with KOH. *Materials Letters*, 15, pp. 15-25.

Dhaneswara, D., Tsania, A., Fatriansyah, J. F., Federico, A., Ulfiati, R., Muslih, R., & Mastuli, M. S. (2024). Synthesis of mesoporous silica from sugarcane bagasse as adsorbent for colorants using cationic and non-ionic surfactants. *International Journal of Technology, 15, 2, pp.* 373-382.

Eddy, N. O., Edet, U. E., Oladele J. O., Kelle, H. I., Ogoko. E. C., Odiongenyi, A. O., Ameh, P., Ukpe, R. A., Ogbodo, R., Garg, R. & Garg, R. (2023f). Synthesis and application of novel microporous framework of nanocomposite from trona for photocatalysed degradation of methyl orange dye. *Environmental Monitoring and Assessment*. doi:10.1007/s10661-023-12014-x,

Eddy, N. O., Garg, R., Garg, R., Aikoye, A. & Ita, B. I. (2022). Waste to resource recovery: mesoporous adsorbent from orange peel for the removal of trypan blue dye from aqueous solution. *Biomass Conversion and Biorefinery*, 13: 13493-13511, doi: 10.1007/s13399-022-02571-5.

Eddy, N. O., Garg, R., Garg, R., Eze, S. I., Ogoko, E. C., Kelle, H. I., Ukpe, R. A., Ogbodo, R. & Chijoke, F. (2023b). Sol-gel synthesis, computational chemistry, and applications of CaO nanoparticles for the remediation of methyl orange contaminated water. *Advances in Nano Research,* https://doi.org/10.12989/anr. -2023.15.1.000.

Eddy, N. O., Garg, R., Garg, R., Garg, R., Ukpe, R. A. & Abugu, H. (2024c). Adsorption and photodegradation of organic contaminants by silver nanoparticles: isotherms, kinetics, and computational analysis. *Environ Monit Assess,* 196, 65, https://doi.org/10.1007/s10661-023-12194-6.

Eddy, N. O., Garg, R., Garg, R., Ukpe, R. A. & Abugu, H. (2023e). Adsorption and photodegradation of organic contaminants by silver nanoparticles: isotherms, kinetics, and computational analysis. *Environmental Monitoring and Assessment*,, D**OI :** 10.1007/s10661-023-12194-6,

Eddy, N. O., Garg, R., Ukpe, R. A., Ameh, P. O., Gar, R., Musa, R., , Kwanchi, D., Wabaidur, S. M., Afta, S., Ogbodo, R., Aikoye, A. O., & Siddiqu, M. (2024b). Application of periwinkle shell for the synthesis of calcium oxide nanoparticles and in the remediation of Pb^{2+}-contaminated water. *Biomass Conversion and Biorefinery*, doi: 10.1007/s13399-024-05285-y

Eddy, N. O., Jibrin, J. I., Ukpe, R. A., Odiongenyi, A. O., Kasiemobi, A. M., Oladele, J. O. & Runde, M. (2024a). Experimental and theoretical investigations of photolytic and photocatalysed degradations of crystal violet dye (cvd) in water by oyster shells derived CaO nanoparticles (CaO-NP), *Journal of Hazardous Materials Advances,* 100413, https://doi.org/10.1016/j.hazadv.2024.100413.

Eddy, N. O., Odiongenyi, A. O., Garg, R., Ukpe, R. A., Garg, R., El Nemir, A., Ngwu, C. M. & Okop, I. J. (2023c). Quantum and experimental investigation of the application of *Crassostrea gasar* (mangrove oyster) shell–based CaO nanoparticles as adsorbent and photocatalyst for the removal of procaine penicillin from aqueous solution. *Environmental Science and Pollution Research*, doi:10.1007/s11356-023-26868-8.

Eddy, N. O., Ukpe, R. A., Garg, R., Garg, R., Odionenyi A. O., Ameh, P. & Akpet, I, N. (2023a). Enhancing Water Purification Efficiency through Adsorption and Photocatalysis: Models, Application and Challenges. *International Journal of Environmental Analytical Chemistry*, DOI: 10.1080/03067319.2023.2295934

Eddy, N. O., Ukpe, R. A., Garg, R., Garg, R., Odiongenyi, A. O., Ameh, P., Akpet, I, N., & Udo, E. S. (2023d). Review of in-depth knowledge on the application of oxides nanoparticles and nanocomposites of Al, Si and Ca as photocatalyst and antimicrobial agents in the treatment of contaminants in water. Clean Technologies and Environmental Policy, doi : 10.1007/s10098-023-02603-2.

Fatima, A., Khan, S., & Rahman, M. (2022). Synthesis of rice husk ash using sol-gel method with KOH. *Journal of Sustainable Materials Research*, 10, 3, pp. 10-20.

Garcia, R., *et al*. (2023). Synthesis and characterization of silicon oxide nanoparticles from coffee grounds for environmental applications. *Journal of Environmental Science and Health, Part B*, *25, 6, pp.* 567-578.

Garg, R., Mittal, M., Tripathi, S., & Eddy, N. O. (2024). Core to concept: synthesis, structure, and reactivity of nanoscale zero-valent iron (NZVI) for wastewater remediation. *Environmental Science and Pollution Research*. Advance online publication. https://doi.org/10.1007/s11356-024-33197-x

Garg, R., Garg, R., Eddy, N. O., Almohana, A. I., Fahad, S., Khan, M. A. & Hong, S. H. (2022). Biosynthesized silica-based zinc oxide nanocomposites for the sequestration of heavy metal ions from aqueous solutions. *Journal of King Saud University*-Science https://doi.org/10.1016/j.jksus.2022.101996

Huang, Y., Wu, Z., & Xu, Q. (2022). Sol-gel synthesis of coconut shelnanoparticles using CTAB surfactant. *Nanotechnology Applications*, 5, 1, pp. 5-15.

Kelle, H. I., Ogoko, E. C., Akintola O & Eddy, N. O. (2023). Quantum and experimental studies on the adsorption efficiency of oyster shell–based CaO nanoparticles (CaONPO) towards the removal of methylene blue dye (MBD) from aqueous solution. Journal: Biomass Conversion and Biorefinery, doi : 10.1007/s13399-023-04947-7.

Kumari, A., Singh, R. K., Kumar, N., Kumari, R., Monalisa, & Sharma, S. (2023). Green synthesis and physical properties of crystalline silica engineering nanomaterial from rice husk (agriculture waste) at different annealing temperatures for its varied applications. *Journal of the Indian Chemical Society*, 100, 5, 100982. https://doi.org/10.1016/j.jics.2023.100982.

Le, T. H., Le, D. T. T., & Tung, N. V. (2021). Synthesis of colloidal silicon quantum dot from rice husk Ash. *Journal of Chemistry,* 2021, 6689590. https://doi.org/10.1155/2021/6689590.

Lee, S., & Park, H. (2020). Microwave-assisted green synthesis of silicon oxide nanoparticles using plant extracts. *Materials Letters*, *30*(4), 267-274.

Li, J., Wang, X., & Zhou, L. (2020). Ball milling approach for wheat straw nanoparticle production. *Journal of Renewable Materials*, 20(4), 20-50.

Li, X., Liu, J., Yang, X., Li, Y., & Zhu, M. (2017). Fabrication of hierarchical macro/mesoporous silica from bamboo leaf ash for efficient adsorption of methylene blue. *RSC Advances*, 7, 17, pp. 10432-10439

Liu, M., & Wang, Q. (2023). Co-precipitation synthesis of silicon oxide nanoparticles using banana peel extract. *Journal of Environmental Nanotechnology*, *15, 4, pp.* 321-330.

Liu, Y., Yao, Z., Li, J., Zhao, Z., & Zhang, S. (2018). Synthesis of mesoporous silica nanoparticles from corncob ash and their application for methylene blue adsorption. RSC Advances, 8, 10, pp. 5902-5911.

Michel, F. M., Meriani, L., Azaïs, T., & Populaire, M. (2011). Revised powder diffraction pattern of synthetic α-quartz (SiO2). Powder Diffraction, 26(2), 221-229. https://www.icdd.com/

Mohammadi, M. R., Davoodi, A. A., & Salari, E. (2020). A review on nano-calcium oxide: Preparation, characterization, and applications. Ceramics International, 46, 13, pp. 19179-19202.

Ogoko, E. C., Kelle, H. I., Akintola, O. & Eddy, N. O. (2023). Experimental and theoretical investigation of *Crasso-*

ostrea gigas (gigas) shells based CaO nanoparticles as a photocatalyst for the degradation of bromocresol green dye (BCGD) in an aqueous solution. *Biomass Conversion and Biorefinery*. https://doi.org/10.1007/s13399-023-03742-8.

Singh, P., Sharma, R., & Gupta, V. (2021). Molten salt method for jute fiber nanoparticle production. *Journal of Sustainable Nanotechnology*, 25, 3, pp. 25-40.

Smith, J., & Johnson, A. (2018). Green synthesis of silicon oxide nanoparticles from plant cvextract. *Journal of Nanoscience*, *10*(2), 123-135.

Umoren, F. J., & Utin, M. C. (2024). Resource recovery from maize wastes: Synthesis and characterization of silicon oxide nanoparticles. *Communication in Physical Sciences, 11*(3), 576-588

Vijayan, R., Kumar, S., & Singh, A. (2023). Ultrasonication-assisted synthesis of banana peel nanoparticles. *Journal of Green Chemistry*, 10(2), 10-20.

Wang, B., Li, X., & Zhang, Y. (2023). Carbothermal reduction of sugarcane bagasse for nanoparticle synthesis. *Environmental Chemistry*, 5, pp. 1-10.

Wang, L., *et al*. (2024). Green synthesis of silicon oxide nanoparticles using tomato fruit extract for antibacterial applications. *Journal of Applied Microbiology*, *36, 2, pp.* 189-198.

Wang, Y., Li, J., Yang, J., & Li, J. (2020). A facile approach for the synthesis of mesoporous silica nanoparticles from sugarcane bagasse ash and their application for dye adsorption. Materials Research Express, 6, 7, pp. 075023.

Xu, H., *et al*. (2023). Chemical vapor deposition synthesis of silicon oxide nanoparticles from bamboo leaf extract. *Journal of Nanoparticle Research*, *18*(9), 789-800.

Xu, Y., Zhao, H., Liu, S., & Shi, J. (2016). Synthesis of ordered mesoporous silica using coconut shell ash as silica source and its application in drug delivery. RSC Advances, 6(11), 9063-9070.

Yang, L., Chen, H., & Wang, J. (2021). Hydrothermal synthesis of bamboo leaf ash nanoparticles with NaOH. *Journal of Biomass Conversion*, 15(2), 15-20.

Yashima, M., Kamiya, K., de Leeuw, N. H., & Minato, H. (2014). First-principles study of the pressure-induced amorphization of cristobalite. Journal of Physics and Chemistry of Solids, 75(1), 70-77. https://www.icdd.com/

Yuan, S., Hou, Y., Liu, C. S., & Ma, Y. (2024). A comparative study on rice husk, as agricultural waste, in the production of silica nanoparticles via different methods. *Materials*, 17(6), 1271. https://doi.org/10.3390/ma17061271.

Zhang, C., Li, X., Liu, J., Sun, Z., & Li, Y. (2013). Synthesis of mesoporous silica nanoparticles from wheat straw ash for methylene blue adsorption. RSC Advances, 3(45), 22748-22757.

Zhang, G., & Li, Y. (2024). Electrochemical synthesis of silicon oxide nanoparticles from onion skin extract. *Journal of Electroanalytical Chemistry*, *40, 7, pp.* 621-632.

Zhang, Q., Liu, W., & Zhao, Z. (2022). Microwave-assisted synthesis of corn straw nanoparticles. *Materials Science and Engineering*, 5, pp. 5-10.

Compliance with Ethical Standards Declaration

Ethical Approval

Not Applicable

Competing interests

The authors declare that they have no known competing financial interests

Funding

This work was supported by Prof. Nnabuk Okon Eddy

Availability of data and materials

Data would be made available on request.

Authors Contribution